Satellite-based assessment of methane emissions from the Darvaza gas crater

Adriana Valverde[1]*, Itziar Irakulis-Loitxate[2,1], Javier Gorroño[1], Zhipeng Pei[3], Javier Roger[1] and Luis Guanter[1,4]

[1] Research Institute of Water and Environmental Engineering (IIAMA), Universitat Politècnica de València, Spain

[2] International Methane Emission Observatory (IMEO), United Nations Environment Programme, Paris, France

[3] State Key Laboratory of Information Engineering in Surveying, Mapping and Remote Sensing, Wuhan University, Wuhan, China

[4] Environmental Defense Fund, Amsterdam, Netherlands

Corresponding author: Adriana Valverde (avaligl@doctor.upv.es)

Key Points:

- The Darvaza gas crater has continuously emitted methane for over 50 years, with total emissions exceeding 900 kt since formation.
- From 2020 to 2025, multiple hyperspectral satellites detected 44 methane plumes above the crater, with emission rates of 0.6–3 t/h.
- We reconstruct the fire history, showing that flaring at the Darvaza crater started between September 1987 and February 1988.

Abstract

Methane is a potent greenhouse gas, and the Darvaza crater in Turkmenistan is a rare, persistent emitter. There are uncertainties regarding its formation date (either 1963 or 1971), fire ignition, and the fire's influence on methane release. Using historical Landsat imagery, we reconstruct the fire history, identifying that combustion began between late 1987 and early 1988. We quantified methane emissions using hyperspectral satellites (EnMAP, PRISMA, EMIT, GF-5A, and ZY-1E), detecting 44 plumes between 2020 and 2025, with 1 to 3 t/h rates. This indicates annual methane emissions of several thousand tonnes, totaling 71 ± 21 kt over five years. Extrapolation suggests cumulative emissions exceed 900 ± 300 kt since formation. Additionally, temporal analysis reveals a gradual decline in flaring intensity, although no apparent correlation with methane was identified. This integrated analysis reduces key uncertainties about the crater's origin and contributes to understanding the long-term natural-anthropogenic methane emissions and their environmental implications.

Plain Language Summary

The Darvaza crater in Turkmenistan, known as "Door to Hell," has been burning for decades and releasing methane, a potent greenhouse gas. However, key details about its history have remained uncertain, including when it formed, when the fire started, and how it affects methane emissions. This study used satellite images to determine that the fire began between late 1987 and early 1988. Using satellite data from 2020 to 2025, we detected 44 distinct methane plumes, with emission rates of 1,000 to 3,000 kilograms per hour. Over five years, the crater released approximately 71,000 tons of methane. Projecting this into the past suggests total emissions exceeding 900,000 tons since the crater formed. Although we observed that the fire has gradually decreased over time, this reduction does not appear to have a clear effect on methane release. Our findings help clarify the crater's history and improve understanding of long-term methane emissions from such unusual sources.

1. Introduction

Methane (CH_4), the primary component of natural gas ,comprising approximately 77–99% by volume (Bahr & Wolff, 2022), is a short-lived but highly potent greenhouse gas. Its global warming potential is approximately 80 times greater than carbon dioxide (CO_2) over a 20-year timeframe (Etminan et al., 2016; Pachauri et al., 2015). The observed increase in atmospheric methane is partly driven by oil and gas exploration, production, and transportation emissions, particularly from leaks, venting, and inefficient flaring across the supply chain (Saunois et al., 2025). This growing concern over methane emissions is particularly relevant in areas with significant natural gas resources (Cusworth et al., 2021; Irakulis-Loitxate et al., 2022).

One such region, the Amu Darya Basin (ADB; Figure 1), in central and eastern Turkmenistan, is a zone of exceptional geological and petroleum significance. Renowned for its abundant oil and gas reserves, the basin extends over 417,000 km² and has accumulated nearly 15 km of sedimentary deposits since the Paleozoic era (Brunet et al., 2017). This region's unique geology has multiple structural and stratigraphic traps facilitating the accumulation of oil and gas reserves. Although extensively explored for its petroleum systems, the ADB exhibits a clear predominance of gas-prone characteristics, with gas fields present throughout all main structural zones, whereas oil discoveries have been restricted to a few small fields (Brunet et al., 2017; Ulmishek, 2004). Specifically, reserve modeling suggests that the total undiscovered resources are estimated at approximately 3.31 billion tons, with gas comprising more than 98% (Ghassemi & Garzanti, 2018). Within the broader context of the ADB, the Karakum High in the northwestern Karakum Desert contains anticlinal folds and faults forming structural traps for hydrocarbon accumulation. Notably, around 20 gas fields have been discovered in this area (Ulmishek, 2004). This rich hydrocarbon province has attracted extensive exploration since the Soviet period, including sulfur works active until the 1960s (Brummell, 2005), adding to its complex environmental profile.

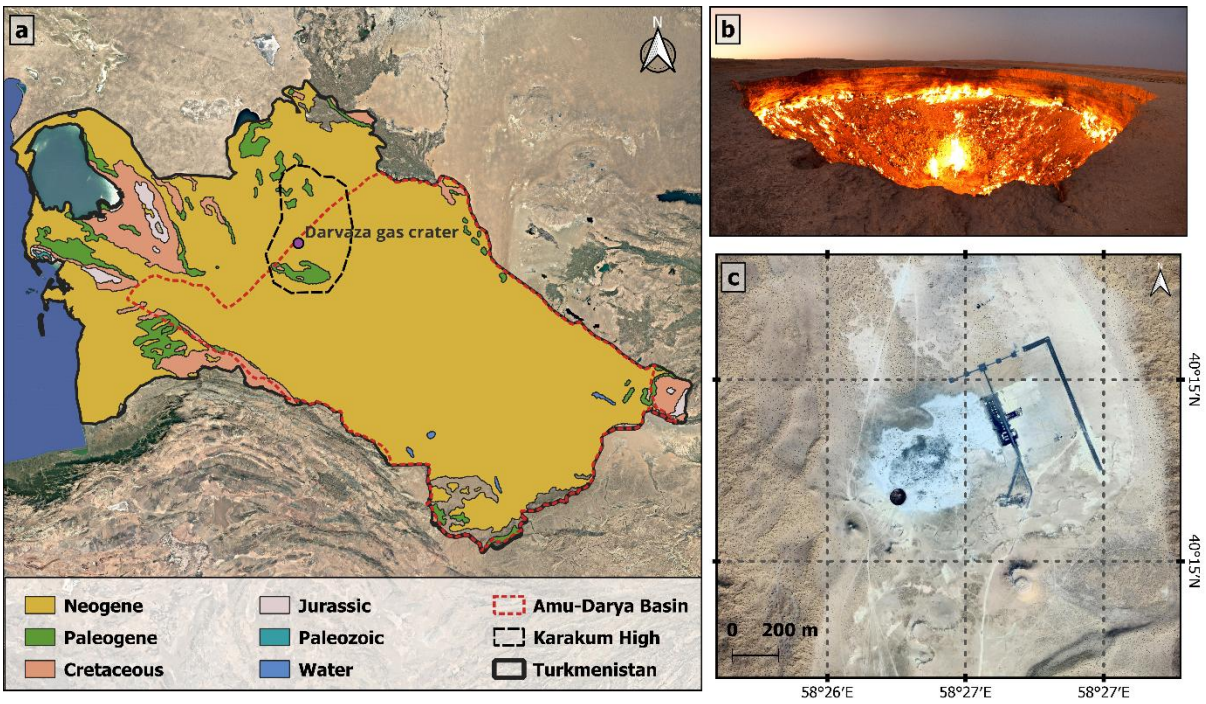

Figure 1. a) Geological map of Turkmenistan showing the location of Darvaza gas crater (purple dot). Map data: Google, © 2025 Airbus. Data source: (Drummer, 1998). b) Ground-level view of the burning Darvaza gas crater. Image: (Sandtorv, 2011). c) A satellite image of the crater area from Google Satellite shows local infrastructure.

The Darvaza gas crater, popularly known as the "Door to Hell", represents a relevant case of interaction between natural processes and anthropogenic activity. According to some studies, the crater's formation can be traced back to 1963, when drilling at the Chaljulba structure of the Zeagli–Derweze field uncovered a gas-filled void, leading to the collapse of the overlying sediments, released a large quantity of methane (Davis, 2024; Pirniyazov & Luryeva, 2024). Conversely, other accounts attribute the crater's creation to an incident in 1971 (Vlasov et al., 2021; Leroy et al., 2022). In either case, a crater was formed approximately 30 meters deep and 60-70 meters in diameter (see Figure S1). Years later, geologists ignited the escaping gas to mitigate the associated hazard, and it has continued to burn for decades, persisting to the present day (Ghassemi & Garzanti, 2018). To date, no rigorous, observation-based assessment of methane emissions from the Darvaza crater has been published. Previous estimates have relied on indirect methods with considerable uncertainty, particularly regarding temporal dynamics and combustion efficiency. More recently, Davis (2024) estimated the total gas flux through the crater at approximately 2.3 t CH_4 per hour. This estimate is based on a satellite-derived flared gas volume of ~2 million standard cubic feet per day, combined with an assumed combustion efficiency of approximately 70%. Under these assumptions, approximately 1.6 t/h would be combusted, and 0.7 t/h would be emitted directly. However, the actual combustion efficiency may be lower, and since the flux estimate is sensitive to this parameter, the resulting figures should be interpreted with caution.

Given that previous assessments of methane emissions have been based on indirect methods, this study aims to detect and quantify the emissions released over the years since the crater's formation using direct satellite observations. Specifically, we employ both hyperspectral and multispectral satellite data to identify and monitor methane plumes. Hyperspectral sensors, due to their high spectral resolution, can detect absorption features specific to methane in the shortwave infrared (SWIR) region, making them well-suited for detecting emission sources. In parallel, multispectral imagery is used to support the temporal reconstruction of key events, such as refining the ignition date of the crater. Although multispectral sensors lack the spectral resolution required to detect weak methane signals, their extensive long-term archives are critical for historical analysis, offering a unique opportunity to reconstruct environmental processes retrospectively over decades (He et al., 2024). By integrating these datasets, we assess the volume of methane emitted and explore its potential correlation with the ongoing fire. Additionally, the study refines the estimation of the crater's ignition date, which is essential for understanding the temporal scale of its environmental impact. This multi-sensor approach demonstrates the capability of satellite remote sensing to support the identification and monitoring of methane emissions in remote regions with limited ground-based observations, such as the Darvaza gas crater.

2. Materials and Methods

2.1. Reconstruction of the crater origin and fire onset from historical Landsat data

To investigate the origin of the crater and the onset of the persistent fire, we began by analyzing historical satellite imagery from the Landsat program, which has been in operation since 1972. The early missions, Landsat 1–3, were equipped with the MSS sensor, which captures four-band images in the visible and near-infrared (NIR) spectrum at a resolution of 57 × 79 meters (resampled to 60 meters in the Landsat Collection 1 Archive). Later missions, Landsat 4–5, carried both the MSS and the TM sensor, which offers seven spectral bands at a higher spatial resolution of 30 meters, and includes thermal and SWIR bands necessary for fire detection, which were unavailable in Landsat 1–3 (Roy et al., 2014). For this study, we obtained the data from the USGS Earth Explorer (USGS science for a changing world, n.d.) , specifically the Landsat 4-5 TM C2 L1 Collection (Earth Resources Observation and Science (EROS) Center, 1982) and focused our analysis on band 7 (SWIR-2, 2.08–2.35 µm) and thermal band 6 (10.4–12.5 µm) from each acquisition (see Figure S2).

2.2. Flaring activity from Fire Information for Resource Management System (FIRMS)

In this study, we used Fire Radiative Power (FRP) data to monitor the intensity of combustion and flaring activity, as it directly measures the radiant energy emitted by fires, making it a key parameter for monitoring flaring events. FRP data was obtained from the Fire Information for Resource Management System (FIRMS) platform, which provides daily observations from the VIIRS sensors onboard the Suomi NPP, NOAA-20 and NOAA-21 satellites (NASA Earthdata, 2025). These data offer diurnal and nocturnal observations at a spatial resolution of 375 m from 2012 to the present. The FIRMS data were downloaded from the NASA FIRMS Archive Download (NASA FIRMS, 2025). In addition, despite its lower sensitivity but given its long historical record, MODIS (Moderate Resolution Imaging Spectroradiometer) data were also downloaded from the FIRMS archive, with MODIS C6.1 data available from November 2000 (for Terra). MODIS provides daily (day and night) global active fire data at 1 km pixel resolution (NASA, 2025). See more information in the SI.

2.3. Detection of methane plumes from hyperspectral data

We have analyzed a dataset composed exclusively of hyperspectral satellite imagery to detect and quantify the methane emissions from the Darvaza gas crater. The combination of surface heterogeneity and the intensity of the emissions, together with the fire signal in the source, makes methane detection by multispectral satellites challenging.

We have obtained 61 images from different instruments (see Table S1). Specifically, the dataset includes 9 from the Advanced Hyperspectral Imager (AHSI) on the Ziyuan-1 (ZY-1E) satellite, 2 from the AHSI on China's Gaofen-5A (GF-5A) satellite, 13 from PRISMA, 9 from EnMAP, and 14 from the EMIT instrument onboard the International Space Station (ISS). These instruments offer high spectral resolution in the SWIR region, including the 1700 nm and 2300 nm spectral windows where methane exhibits distinct absorption features suitable for remote detection and quantification.

EnMAP, PRISMA, and EMIT have demonstrated strong capabilities for methane emission detection, supported by their spectral coverage in the SWIR (Guanter et al., 2021; Roger et al., 2024; Thorpe et al., 2023). These instruments combine suitable spectral resolution with moderate spatial sampling (30 m for EnMAP and PRISMA; 60 m for EMIT), enabling reliable plume identification. However, the availability of data from those missions is low due to their sparse spatio-temporal sampling. Our dataset was also obtained from two versions of the AHSI instruments onboard China's GF-5A and ZY-1E satellites (Irakulis-Loitxate et al., 2021; Liu et al., 2019; Yan et al., 2022). These hyperspectral platforms provide moderate spatial resolution and wide swath coverage, making them ideal for regional assessments, although their signal-to-noise ratio and radiometric calibration may limit precise plume detection.

2.4. Quantification of methane emissions

We derived methane concentration enhancement (ΔXCH_4) maps from the hyperspectral L1B radiance data using a matched-filter retrieval algorithm (Thompson et al., 2016) adapted to each sensor's spectral configuration. Visual inspections of the resulting ΔXCH_4 maps were conducted to identify plume-like structures. These were then cross-referenced with high-resolution base maps from Google Earth to exclude retrieval artifacts and confirm the source of the plume. Additionally, we verify the coherence between observed plume orientation and the wind speed at 10 m above the surface (U10) derived from the NASA Goddard Earth Observing System-Fast Processing (GEOS-FP) meteorological reanalysis product (Molod et al., 2012). The GEOS-FP U10 product has a temporal resolution of 1 hour. In our analysis, wind data were linearly interpolated between the nearest hourly values. A comparison between GEOS-FP and ERA5-Land wind data (Muñoz Sabater, J., 2019) (Figures S3–S4) showed that the differences did not significantly affect the emission estimates. Finally, we applied the Integrated Methane Enhancement (IME) method to quantify methane emissions, translating column concentration into emission fluxes (Frankenberg et al., 2016; Varon et al., 2018). Subsequently, to estimate total emissions over the 2020–2025 period, we fit a second-degree polynomial to the time series of flux estimates and integrated the resulting curve. Uncertainty in the total emission estimate was assessed via Monte Carlo simulations. See more information in the SI.

3. Results and Discussion

3.1. Reconstructing the history of the crater using historical satellite observations

There has been ongoing disagreement in available sources regarding the formation date of the crater. Various sources report differing dates for the crater's formation, with some indicating 1963 (Davis, 2024; Pirniyazov & Luryeva, 2024) and others suggesting 1971 (Leroy et al., 2022; Vlasov et al., 2021).What can be conclusively established is that the crater was already present by October 25, 1972, based on the analysis of a Landsat 1 image, which clearly shows the crater. However, the exact year of its formation remains uncertain, and it is not possible to determine whether the crater was formed shortly before this date or significantly earlier.

To approximate the onset of flaring activity at the Darvaza gas crater, an essential factor in determining whether methane emissions were combusted or directly emitted, we conducted an analysis of satellite imagery from the Landsat 4–5 Thematic Mapper (TM) missions covering the period 1984-1988. Notably, thermal data from Band 6 (thermal infrared - TIR) and Band 7 revealed no sustained thermal anomalies indicative of active flaring between 1984 and early 1988. This absence of thermal signatures persisted until a change was observed between September 1987 and February 1988, when the onset of flaring was detected (Figure 2). This finding, which provides the first temporal constraint on the ignition of the crater, refines previous estimates suggesting that burning may not have begun until the 1980s (Johnson, 2024). Since

that point, the crater has burned continuously, exhibiting combustion behavior similar to industrial gas flaring, but unlike typical flares, it is not static. The crater, approximately 60–70 meters in diameter, exhibits dynamic flame movement along various surface fissures and vents within the cavity (see Figure 2). The subsurface comprises alternating sedimentary layers, aquifers, and denser formations that may facilitate sustained gas migration toward the surface (Ghassemi & Garzanti, 2018), suggesting that emissions may not originate from a single reservoir but from multiple subsurface gas sources contributing to persistent combustion. In this context, the onset of flaring represents not only a visible transformation of the crater but also a critical shift in its emission behavior; in the absence of combustion, the gas, primarily methane, would likely have been released directly into the atmosphere, resulting in substantially higher atmospheric methane emissions than those estimated during the active flaring period.

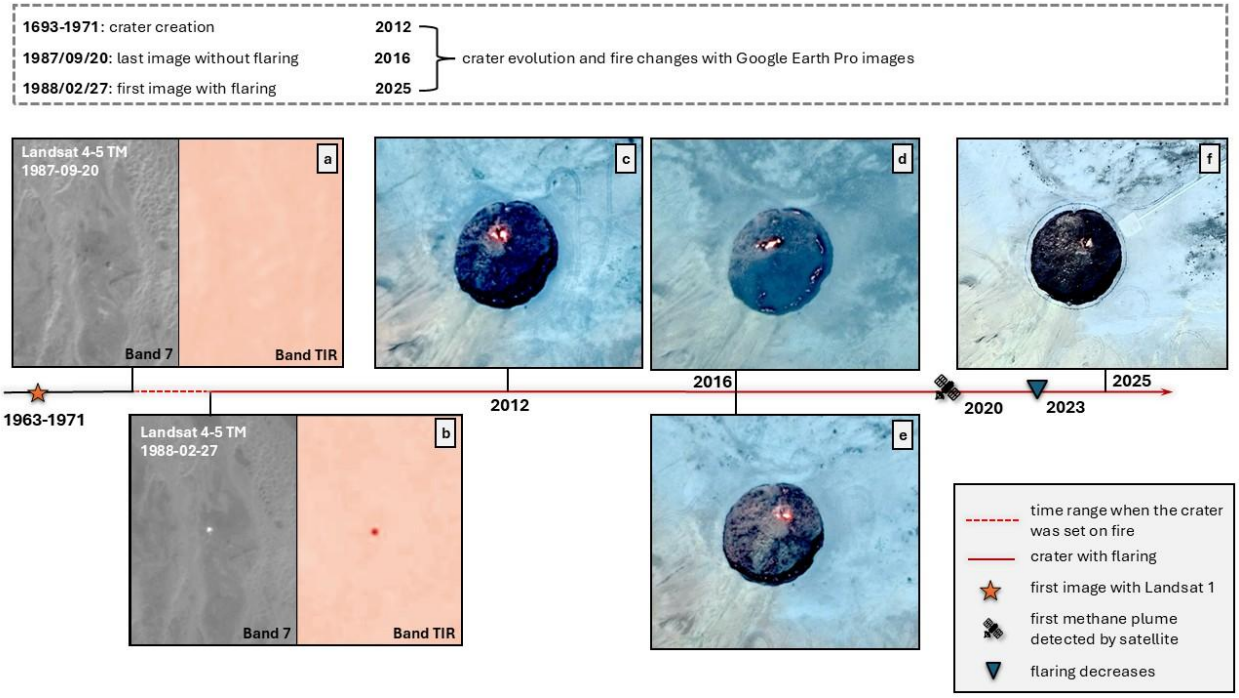

Figure 2. The timeline of the Darvaza gas crater is based on satellite observations. The top section summarizes key events: crater formation (1963 or 1971), the last satellite image without flaring (1987/09/20), and the first image showing flaring (1988/02/27), and from 2012 to 2025, the crater's evolution and fire activity were monitored using Google Earth Pro high-resolution imagery. Panels (a) and (b) show Landsat 5 TM images, with Band 7 in grayscale and Band 6 (thermal infrared) in orange tones; thermal activity is absent in 1987 but clearly visible in 1988. Panels (c) through (f) depict the crater's evolution and varying fire intensity from 2012 to 2025 ((c), (d), (e) Google, © 2025 Maxar Technologies; (f) Google, © 2025 Airbus). Symbols in the bottom right legend mark key events: the first Landsat detection (1971), the onset of flaring in early 1988, the first satellite-based methane plume detection (2020), and a visible decrease in flaring activity by 2023.

3.2. Detection of methane plumes using hyperspectral satellite data between 2020 and 2025

Owing to the lack of long-term historical hyperspectral satellite records - unlike the extensive archives of multispectral systems such as Landsat - our analysis of methane emissions over Darvaza Crater is limited to recent observations from 2020 onwards. Between April 2020 and May 2025, 44 methane plumes were identified over the Darvaza crater region in Turkmenistan using imagery from various hyperspectral satellite missions. Specifically, 6 plumes were detected by ZY-1E, 2 by GF-5A, 13 by PRISMA, 9 by EnMAP, and 14 by EMIT (see Table S2), the first confirmed detection recorded by ZY-1E in April 2020 (Figure 3), with an emission of 1.8 ± 0.7 t/h. The highest methane emission was detected by ZY-1E on 22 August 2023, with an estimated rate of 3.18 ± 1.20 t/h. This value closely aligns with a subsequent observation by EMIT three days later, which recorded a similar emission rate of 3.16 ± 1.28 t/h, reinforcing the temporal consistency of high-intensity release events. A comparable pattern was observed on 15 October 2024, when PRISMA and EnMAP detected plumes with closely matching magnitudes, 1.3 ± 0.4 t/h and 1.2 ± 0.4 t/h, respectively (see more examples in SI, Figure S5). Conversely, the lowest emission recorded was 632 ± 230 kg/h, measured by EMIT in July 2024. See the detection time series in Figure 3.

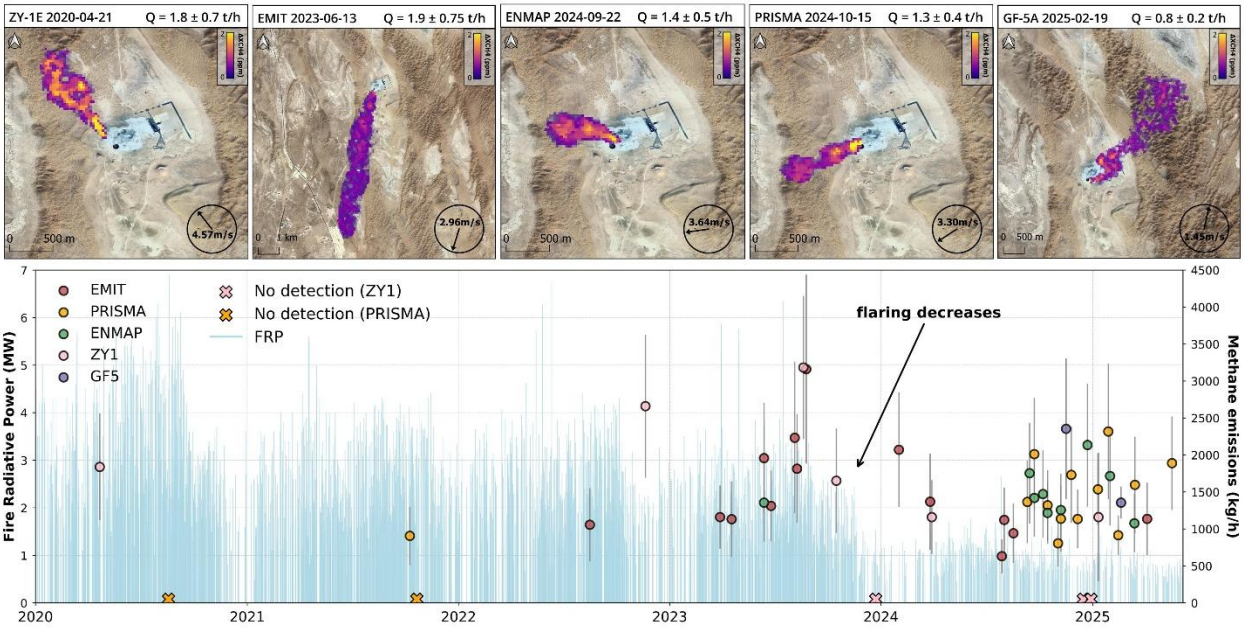

Figure 3. Time series of methane plumes and flaring activity at the Darvaza crater. In the upper panels, examples of methane plumes from different satellites on different dates. Map background: Google Satellite. At the bottom, historical flaring analysis using only VIIRS (NASA FIRMS, 2025) and the time series of the detected plumes with their emission flux rate estimates and the uncertainty represented as vertical error bars (see Table S2 for more information).

These observations reveal significant variability in emission intensities (from ~0.6 to 3 t/h), consistent with the dynamic nature of gas release from geological features like this crater. Additionally, multiple factors influence both the detectability and quantification of methane plumes from satellite observations. Meteorological variables such as wind speed and direction can significantly alter plume shape, dispersion, and column concentration, thus impacting satellite-based retrievals. Furthermore, it is critical to consider the high frequency of dust storms in the Karakum Desert, which records the highest incidence of dust storms in Central Asia, with more than 40 events annually (Ghassemi & Garzanti, 2018). These dust storms can significantly increase atmospheric aerosol load, introducing additional scattering and absorption in the SWIR spectral region (Kambezidis & Kaskaoutis, 2008). Besides, meteorological conditions such as rainfall or snow cover during winter can significantly affect the surface radiance and the level of the crater's fire, although such weather events are relatively infrequent, occurring on fewer than 40 days per year (Weather Atlas, 2024). For these reasons, we highlight that lack of detection does not necessarily indicate the absence of emissions but reflects the complex interplay between source behavior, atmospheric conditions, surface reflectance, and instrumental sensitivity. This complexity is particularly evident in the analysis of certain ZY-1E and PRISMA acquisitions, where no plumes were detected despite the probability of ongoing emissions (see Table S3). The absence of plumes in these 5 images can be attributed to the timing of the acquisitions, which may have been unfavorable for detection. Specifically, one ZY-1E image was captured during strong winds (>11.5 m/s), and several others under relatively high wind conditions.

Additionally, a reduction in flaring was observed after summer 2023 (see Figures S6-S7); however, no clear correlation has been found between this reduction and the intensity of methane emissions (see Text S5 and Figure S8). These observations suggest that part of the gas may be released directly into the atmosphere through multiple subsurface fissures, bypassing combustion. While some of the methane is visibly flared, a significant portion may escape unburned due to the complex geological structure of the crater, which probably includes diffuse venting pathways, potentially explaining the lack of correlation between flaring intensity and methane emission.

In parallel with these observations, recent efforts have focused on mitigation through subsurface intervention in response to persistent methane emissions. Specifically, scientists have proposed drilling a well at the Chaldzhulba field to intercept gas-bearing formations between 200 and 950 meters deep to mitigate methane emissions from the crater. This action would allow controlled extraction and gradual gas flow redirection, reducing uncontrolled emissions (Davis, 2024). Our VIIRS FRP analysis (Figure 3) shows a gradual decline in flaring intensity beginning around 2018–2019, followed by an accelerated decrease after summer 2023, consistent with the period during which mitigation through subsurface drilling was reported (Oilgas, 2022; Pirniyazov & Luryeva,

2024). This trend is corroborated by satellite-based flaring data from Capterio (Davis, 2024), which also indicates a significant reduction in visible burning from September 2023 onward.

3.3. Estimation of total emissions from the crater

In our study, we provide a direct assessment based on hyperspectral satellite observations. We interpret the crater's emission history as comprising three distinct periods: (i) 2020–2025, during which methane emissions were directly observed and quantified; (ii) 1988–2019, during which flaring was likely continuous but the methane not directly measured; and (iii) 1963–1987, when no flaring systems were present and all associated emissions are assumed to have been released as uncombusted methane.

For the most recent period (2020–2025), we estimate total methane emissions of 71 ± 21 kt CH_4 based on plume detections using hyperspectral satellite observation (see more information about the estimation of total emissions in Figures S9-S10). This estimate is currently the most reliable, grounded in direct observational data and would correspond to approximately 6.0 Mt CO_2-equivalent under a 20-year global warming potential (Pachauri et al., 2015), underscoring the substantial short-term climate impact of the observed emissions. For context, this emission level is comparable to major accidental releases such as the Aliso Canyon event in California, which released approximately 97 kt CH_4 over four months (Conley et al., 2016), and the blowout in Kazakhstan, which is estimated at 131 ± 34 kt CH_4 over a period of 6 months (Guanter et al., 2024). Assuming the crater was formed in 1971, and emissions have remained stable, we have extrapolated potential emissions to approximately 800 ± 250 kt CH_4. However, if the formation year is considered to be 1963, a total period of 62 years, this estimate could increase up to 900 ± 300 kt CH_4. Notably, this estimation should be regarded as highly conservative, as emissions during the initial pre-flaring phase were likely substantially higher. Furthermore, this estimate accounts solely for methane emissions and does not include methane that was combusted.

4. Conclusion

The Darvaza gas crater represents one of the most intriguing natural-anthropogenic geological features globally. Since its formation, estimated to be in either 1963 or 1971, the site has continuously released substantial quantities of methane into the atmosphere. The geological configuration of the crater, characterized by alternating sedimentary strata and aquifers, facilitates upward gas migration and persistent emissions originating from multiple subsurface reservoirs.

This study analyzed the history of the crater using the Landsat 1–5 satellite data archive, determining that flaring at the crater began between September 1987 and February 1988. This represents a novel finding, as no prior study had established ignition timing with such temporal

resolution. This temporal constraint is critical for reconstructing the history of emissions, as it implies that during the pre-flaring period, all methane was vented directly into the atmosphere without combustion. Consequently, emissions during this period would be higher than those recorded during active flaring years.

Furthermore, over the past five years, hyperspectral satellite imagery - including EnMAP, PRISMA, EMIT, GF-5A and ZY-1E - has identified 44 methane plumes above the crater, with emission rates varying from approximately 0.6 to over 3 t/h. Although a reduction in flaring activity was observed during the summer of 2023, no consistent correlation was found between flaring intensity and methane release. This suggests that a substantial fraction of the gas escapes combustion, likely via diffuse or bypassing subsurface venting pathways, and that the proposed activity of drilling wells in nearby fields to reduce the gas flow to the crater would be impacting the amount of gas flared but not the gas vented. Moreover, the continued flaring and venting of large gas volumes represent a missed opportunity for energy utilization.

Finally, total methane emissions with direct satellite observations are estimated at 71 ± 21 kt CH_4 for 2020–2025. Extending this analysis to the entire lifetime of the Darvaza crater, we estimate cumulative emissions of at least 800 ± 300 kt CH_4, depending on its year of creation, could have reached 900 kt. This value represents a conservative lower bound, as it does not account for potentially higher emissions during the early, pre-flaring decades. These findings underscore the critical value of integrating high-resolution hyperspectral satellite data with historical activity records to constrain methane sources' long-term climate impact accurately.

The broader implications extend beyond the singular case of Darvaza. Persistent, uncontrolled methane sources -natural, anthropogenic, or hybrid- drive near-term climate forcing and are likely underrepresented in greenhouse-gas inventories. Although Darvaza's remote desert location limits local impacts, analogous emitters (mud volcanoes, blowouts, leaking fields) can occur near populations or sensitive ecosystems, degrading air quality, threatening biodiversity, and endangering health. Mitigation will require integrating high-resolution satellite monitoring into regulatory frameworks, incentivizing gas capture through economic or carbon-credit mechanisms, and mapping leakage-prone geologic structures. Coordinated campaigns using hyperspectral satellites, aircraft, and ground surveys could improve the temporal resolution of emissions, refine estimates of cumulative climate impact, and guide intervention scenarios ranging from engineered sealing to energy recovery.

Notably, Turkmenistan, identified by satellites as a hotspot of methane "super-emitter" events, joined the Global Methane Pledge at COP28 (Global Methane Pledge Homepage, n.d.; Ministry of Foreign Affairs of Turkmenistan, 2023) and in 2024 designated a focal point to receive alerts from UNEP's Methane Alert and Response System (MARS)(United Nations Environment

Programme, n.d.). MARS is a satellite-based detection and notification service that issues plume-level alerts to governments and operators for rapid verification and follow-up. Since then, MARS notifications for Turkmenistan have elicited feedback from government agencies and asset operators for more than 20 discrete emission point-source, with commitments to investigate and respond to additional outstanding alerts(United Nations Environment Programme, 2024). Timely detection and attribution thus matter: they permit targeted, asset-level responses and provide credible verification of mitigation progress. For this reason, the case of the Darvaza crater exemplifies the potential of Earth observation tools to uncover and quantify emissions from long-lived, poorly monitored sources, highlighting the need to incorporate such forgotten sites into regional and global inventories to enable effective mitigation strategies.

Acknowledgments

We thank the Italian Space Agency (ASI) and the German Aerospace Center (DLR) for facilitating the PRISMA and EnMAP acquisitions, respectively. We also acknowledge NASA's Jet Propulsion Laboratory team for providing EMIT data and maintaining the Landsat program. In addition, we are grateful to Daniel Varon for supplying the WRF-LES wind simulations used in this study. The authors thank the China Centre for Resources Satellite Data and Application for the GF-5A and ZY-1 data used in this study. This research is partly funded by the ESA MEDUSA project (ESA Contract No. 4000143908/24/I-LR). Itziar Irakulis-Loitxate is funded by UNEP's International Methane Emissions Observatory (IMEO).

Conflict of Interest

The authors declare there are no conflicts of interest for this manuscript.

Author contributions

Conceptualization: All authors. Methodology: A. V., I. I. and L. G. Formal Analysis: All authors. Investigation: A. V. and I.I. Supervision: L G. Writing-original draft: A. V. Writing-review and editing: All authors.

Availability Statement

The data from GF-5A and ZY-1E are available in the Zenodo repository associated with this work (Valverde et al., 2026). The other satellite datasets used in this study are publicly available

through their respective data portals. Landsat 1–5 MSS Collection 2 Level 1 are available from the USGS EarthExplorer portal (https://earthexplorer.usgs.gov/**,** Earth Resources Observation and Science (EROS) Center, 1972) and Landsat 4–5 TM Collection 2 Level 1 are also available from the USGS EarthExplorer portal (https://earthexplorer.usgs.gov/, Earth Resources Observation and Science (EROS) Center, 1982). PRISMA L1B images are publicly available at https://prisma.asi.it/, which requires free registration at https://prismauserregistration.asi.it/. EnMAP L1B images are available from the German Aerospace Center through the EnMAP Instrument Planning Portal (https://planning.enmap.org/), which requires free registration at https://sso.eoc.dlr.de/enmap/selfservice/public/newuser. EMIT L1B images available at NASA Land Processes Distributed Active Archive Center (Green, 2022). VIIRS (NOAA-20, VIIRS NOAA-21 and Suomi-NPP) and MODIS Terra are available at the Fire Information for Resource Management System (FIRMS) platform (https://firms.modaps.eosdis.nasa.gov/download/, (NASA FIRMS, 2025). The reanalysis wind data from GEOS-FP data (*u* and *v* components) were obtained from the NASA Global Modeling and Assimilation Office (GMAO) data portal (https://portal.nccs.nasa.gov/datashare/gmao/geos-fp/das/, Molod et al., 2012). ERA5-Land hourly data from 1950 to present are obtained from the European Centre for Medium-Range Weather Forecasts (Muñoz Sabater, J., 2019). The core analytical code for plume masking, delineation, and IME-based flux quantification is publicly available at https://github.com/jarojuan96/HS_CH4_Emission_Quantification. The satellite-specific methane retrieval follows the well-established matched-filter methodology, for which several publicly available implementations exist: https://github.com/markusfoote/mag1c, https://github.com/UNEP-IMEO-MARS/marshsi/tree/main/marshsi, and https://github.com/sron-esg/hypergas.

Supporting Information

Additional figures, data tables, and methods used to estimate methane emissions from the Darvaza crater are provided in the Supporting Information.

References

Bahr, M.-S., & Wolff, M. (2022). PAS-based isotopologic analysis of highly concentrated methane. *Frontiers in Environmental Chemistry*, *3*, 1029708. https://doi.org/10.3389/fenvc.2022.1029708

Brummell, P. (2005). *Turkmenistan: the Bradt travel guide*. Chalfont St. Peter: Bradt Travel Guides.

Brunet, M.-F., Ershov, A. V., Korotaev, M. V., Melikhov, V. N., Barrier, E., Mordvintsev, D. O., & Sidorova, I. P. (2017). Late Palaeozoic and Mesozoic evolution of the Amu Darya Basin (Turkmenistan, Uzbekistan). *Geological Society, London, Special Publications*, *427*(1), 89–144. https://doi.org/10.1144/SP427.18

Capterio. (n.d.). FlareIntel: A digital tool to track and reduce global gas flaring. Retrieved from https://flareintel.com/

Conley, S., Franco, G., Faloona, I., Blake, D. R., Peischl, J., & Ryerson, T. B. (2016). Methane emissions from the 2015 Aliso Canyon blowout in Los Angeles, CA. *Science*, *351*(6279), 1317–1320. https://doi.org/10.1126/science.aaf2348

Cusworth, D. H., Duren, R. M., Thorpe, A. K., Olson-Duvall, W., Heckler, J., Chapman, J. W., et al. (2021). Intermittency of Large Methane Emitters in the Permian Basin. *Environmental Science & Technology Letters*, *8*(7), 567–573. https://doi.org/10.1021/acs.estlett.1c00173

Davis, M. (2024, April 23). A New Perspective on Old Flames: Satellite Tracking of Emissions Reduction at the 60-Year Darvaza Fire Crater in Turkmenistan. Retrieved from https://flareintel.com/insights/a-new-perspective-on-old-flames-satellite-tracking-of-emissions-reduction-at-the-60-year-darvaza-fire-crater-in-turkmenistan#_ftn7

Drummer, T. D. (1998). Generalized Geology of the Former Soviet Union (geo1ec) [Data set]. U.S. Geological Survey. https://doi.org/10.5066/P9GUL0PQ

Earth Resources Observation and Science (EROS) Center. (1972). Landsat 1-5 Multispectral Scanner Level-1, Collection 1 [Tiff]. U.S. Geological Survey. https://doi.org/10.5066/F7H994GQ

Earth Resources Observation and Science (EROS) Center. (1982). Landsat 4-5 Thematic Mapper Level-1, Collection 2 [Other]. U.S. Geological Survey. https://doi.org/10.5066/P918ROHC

Etminan, M., Myhre, G., Highwood, E. J., & Shine, K. P. (2016). Radiative forcing of carbon dioxide, methane, and nitrous oxide: A significant revision of the methane radiative forcing. *Geophysical Research Letters*, *43*(24), 12,614-12,623. https://doi.org/10.1002/2016GL071930

Frankenberg, C., Thorpe, A. K., Thompson, D. R., Hulley, G., Kort, E. A., Vance, N., et al. (2016). Airborne methane remote measurements reveal heavy-tail flux distribution in Four Corners region. *Proceedings of the National Academy of Sciences*, *113*(35), 9734–9739. https://doi.org/10.1073/pnas.1605617113

Ghassemi, M. R., & Garzanti, E. (2018). Geology and geomorphology of Turkmenistan: A review. *Geopersia*, *9(1)*(Online First), 125–140. https://doi.org/10.22059/geope.2018.265613.648416

Global Methane Pledge Homepage. (n.d.). Global Methane Pledge. Retrieved August 19, 2025, from https://www.globalmethanepledge.org/

Green, R. (2022). EMIT L1B At-Sensor Calibrated Radiance and Geolocation Data 60 m V001 [Data set]. NASA Land Processes Distributed Active Archive Center. https://doi.org/10.5067/EMIT/EMITL1BRAD.001

Guanter, L., Irakulis-Loitxate, I., Gorroño, J., Sánchez-García, E., Cusworth, D. H., Varon, D. J., et al. (2021). Mapping methane point emissions with the PRISMA spaceborne imaging spectrometer. *Remote Sensing of Environment*, *265*, 112671. https://doi.org/10.1016/j.rse.2021.112671

Guanter, L., Roger, J., Sharma, S., Valverde, A., Irakulis-Loitxate, I., Gorroño, J., et al. (2024). Multisatellite Data Depicts a Record-Breaking Methane Leak from a Well Blowout. *Environmental Science & Technology Letters*, *11*(8), 825–830. https://doi.org/10.1021/acs.estlett.4c00399

He, T.-L., Boyd, R. J., Varon, D. J., & Turner, A. J. (2024). Increased methane emissions from oil and gas following the Soviet Union's collapse. *Proceedings of the National Academy of Sciences*, *121*(12), e2314600121. https://doi.org/10.1073/pnas.2314600121

Irakulis-Loitxate, I., Guanter, L., Liu, Y.-N., Varon, D. J., Maasakkers, J. D., Zhang, Y., et al. (2021). Satellite-based survey of extreme methane emissions in the Permian basin. *Science Advances*, *7*(27), eabf4507. https://doi.org/10.1126/sciadv.abf4507

Irakulis-Loitxate, I., Guanter, L., Maasakkers, J. D., Zavala-Araiza, D., & Aben, I. (2022). Satellites Detect Abatable Super-Emissions in One of the World's Largest Methane Hotspot Regions. *Environmental Science & Technology*, *56*(4), 2143–2152. https://doi.org/10.1021/acs.est.1c04873

Johnson, C. (2024, August 19). What It's Like at the Real-Life 'Gates of Hell' in Turkmenistan. Retrieved from https://www.mentalfloss.com/posts/turkmenistan-gates-of-hell

Kambezidis, H. D., & Kaskaoutis, D. G. (2008). Aerosol climatology over four AERONET sites: An overview. *Atmospheric Environment*, *42*(8), 1892–1906. https://doi.org/10.1016/j.atmosenv.2007.11.013

Leroy, S. A. G., Gracheva, R., & Medvedev, A. (2022). Natural hazards and disasters around the Caspian Sea. *Natural Hazards*, *114*(3), 2435–2478. https://doi.org/10.1007/s11069-022-05522-5

Liu, Y.-N., Zhang, J., Zhang, Y., Sun, W.-W., Jiao, L.-L., Sun, D.-X., et al. (2019). The Advanced Hyperspectral Imager: Aboard China's GaoFen-5 Satellite. *IEEE Geoscience and Remote Sensing Magazine*, *7*(4), 23–32. https://doi.org/10.1109/MGRS.2019.2927687

Ministry of Foreign Affairs of Turkmenistan. (2023, December 1). Turkmenistan joined the Global Methane Pledge [Press Release]. Retrieved August 19, 2025, from https://www.mfa.gov.tm/en/news/4242

Molod, A., Takacs, L., Suarez, M., Bacmeister, J., Song, I.-S., & Eichmann, A. (2012). The GEOS-5 atmospheric general circulation model: mean climate and development from MERRA to fortuna. Retrieved from https://portal.nccs.nasa.gov/datashare/gmao/geos-fp/das/

Muñoz Sabater, J. (2019). ERA5-Land hourly data from 1950 to present [Data set]. Copernicus Climate Change Service (C3S) Climate Data Store (CDS). https://doi.org/10.24381/CDS.E2161BAC

NASA. (2025). MODIS Standard Collection 6.1 Update. Retrieved from https://atmosphere-imager.gsfc.nasa.gov/documentation/collection-61

NASA Earthdata. (2025). VIIRS (Visible Infrared Imaging Radiometer Suite). Retrieved from https://www.earthdata.nasa.gov/data/instruments/viirs

NASA FIRMS. (2025). FIRMS fire map: VIIRS active fire data (NOAA-21) [[Dataset]]. Retrieved from https://firms.modaps.eosdis.nasa.gov/map/

Oilgas. (2022, June 24). Scientists of Turkmenistan have developed a way to take control of the Darvaza crater. Retrieved from https://oilgas.gov.tm/en/posts/habarlar/4895/turkmenistanyn-alymlary-derweze-kraterini-goz-astyna-almagyn-usulyny-islap-duzduler

Pachauri, R. K., Mayer, L., & Intergovernmental Panel on Climate Change (Eds.). (2015). *Climate change 2014: synthesis report*. Geneva, Switzerland: Intergovernmental Panel on Climate Change.

Pirniyazov, B. K., & Luryeva, I. I. (2024, April 15). The method of reducing methane emissions from the Derweze crater, proposed by Turkmen scientists, has received practical confirmation. Retrieved from https://orient.tm/en/post/71298/method-reducing-methane-emissions-derweze-crater-proposed-turkmen-scientists-has-received-practical-confirmation

Roger, J., Irakulis-Loitxate, I., Valverde, A., Gorroño, J., Chabrillat, S., Brell, M., & Guanter, L. (2024). High-Resolution Methane Mapping With the EnMAP Satellite Imaging Spectroscopy Mission. *IEEE Transactions on Geoscience and Remote Sensing*, *62*, 1–12. https://doi.org/10.1109/TGRS.2024.3352403

Roy, D. P., Wulder, M. A., Loveland, T. R., C.E., W., Allen, R. G., Anderson, M. C., et al. (2014). Landsat-8: Science and product vision for terrestrial global change research. *Remote Sensing of Environment*, *145*, 154–172. https://doi.org/10.1016/j.rse.2014.02.001

Sandtorv, T. (2011). Darvasa gas crater panorama [Cropped photograph]. Retrieved April 5, 2025, from . https://commons.wikimedia.org/wiki/File:Darvasa_gas_crater_panorama.jpg

Saunois, M., Martinez, A., Poulter, B., Zhang, Z., Raymond, P. A., Regnier, P., et al. (2025). Global Methane Budget 2000–2020. *Earth System Science Data*, *17*(5), 1873–1958. https://doi.org/10.5194/essd-17-1873-2025

Thompson, D. R., Thorpe, A. K., Frankenberg, C., Green, R. O., Duren, R., Guanter, L., et al. (2016). Space-based remote imaging spectroscopy of the Aliso Canyon CH_4 superemitter. *Geophysical Research Letters*, *43*(12), 6571–6578. https://doi.org/10.1002/2016GL069079

Thorpe, A. K., Green, R. O., Thompson, D. R., Brodrick, P. G., Chapman, J. W., Elder, C. D., et al. (2023). Attribution of individual methane and carbon dioxide emission sources using EMIT observations from space. *Science Advances*, *9*(46), eadh2391. https://doi.org/10.1126/sciadv.adh2391

Ulmishek, G. F. (2004). Petroleum geology and resources of the Amu-Darya basin, Turkmenistan, Uzbekistan, Afghanistan, and Iran. *USGS Numbered Series*, 38. https://doi.org/10.3133/b2201H

United Nations Environment Programme. (2024). *An Eye on Methane — Invisible but not unseen: How data-driven tools can turn the tide on methane emissions – if we use them*. United Nations Environment Programme. https://doi.org/10.59117/20.500.11822/46541

United Nations Environment Programme. (n.d.). Methane Alert and Response System (MARS). Retrieved August 19, 2025, from https://www.unep.org/topics/energy/methane/methane-alert-and-response-system-mars

USGS science for a changing world. (n.d.). Earth Explorer. Retrieved January 5, 2025, from https://earthexplorer.usgs.gov/

Valverde, A., Irakulis Loitxate, I., Gorroño, J., Pei, Z., & Guanter, L. (2026). Level-1B data from ZY-1E and GF-5A for Darvaza gas crater [Data set]. Zenodo. https://doi.org/10.5281/ZENODO.19066150

Varon, D. J., Jacob, D. J., McKeever, J., Jervis, D., Durak, B. O. A., Xia, Y., & Huang, Y. (2018). Quantifying methane point sources from fine-scale satellite observations of atmospheric methane plumes. *Atmospheric Measurement Techniques*, *11*(10), 5673–5686. https://doi.org/10.5194/amt-11-5673-2018

Vlasov, S., Konovalova, O., Chudovskaya, I., Vlasova, I., Kolotilova, N., & Snakin, V. (2021). *Methane in the atmosphere, methanotrophs and development of oil and gas industry*. LLC MAKS Press. https://doi.org/10.29003/m1986.978-5-317-06580-5

Weather Atlas. (2024, August 2). Climate and monthly weather forecast Darvaza, Turkmenistan. Retrieved from https://www.weather-atlas.com/en/turkmenistan/darvaza-climate

Yan, L., Li, J., & Xiao, C. (2022). Vicarious Radiometric Calibration of the AHSI Instrument Onboard ZY1E on Dunhuang Radiometric Calibration Site. *IEEE Transactions on Geoscience and Remote Sensing*, *60*, 1–13. https://doi.org/10.1109/TGRS.2022.3180120

Supporting References

Caseiro, A., Rücker, G., Tiemann, J., Leimbach, D., Lorenz, E., Frauenberger, O., & Kaiser, J. W. (2018, May 2). A Methodology for Gas Flaring Detection and Characterisation Using SLSTR. https://doi.org/10.20944/preprints201805.0020.v1

Copernicus Climate Change Service. (2019). ERA5-Land hourly data from 1950 to present [Data set]. Copernicus Climate Change Service (C3S) Climate Data Store (CDS). https://doi.org/10.24381/CDS.E2161BAC

Drummer, T. D. (1998). Generalized Geology of the Former Soviet Union (geo1ec) [Data set]. U.S. Geological Survey. https://doi.org/10.5066/P9GUL0PQ

Fu, Y., Li, R., Wang, X., Bergeron, Y., Valeria, O., Chavardès, R. D., et al. (2020). Fire Detection and Fire Radiative Power in Forests and Low-Biomass Lands in Northeast Asia: MODIS versus VIIRS Fire Products. *Remote Sensing*, *12*(18), 2870. https://doi.org/10.3390/rs12182870

Schroeder, W., Oliva, P., Giglio, L., & Csiszar, I. A. (2014). The New VIIRS 375 m active fire detection data product: Algorithm description and initial assessment. *Remote Sensing of Environment*, *143*, 85–96. https://doi.org/10.1016/j.rse.2013.12.008

Wooster, M. J., Roberts, G., Perry, G. L. W., & Kaufman, Y. J. (2005). Retrieval of biomass combustion rates and totals from fire radiative power observations: FRP derivation and calibration relationships between biomass consumption and fire radiative energy release. *Journal of Geophysical Research: Atmospheres*, *110*(D24), 2005JD006318. https://doi.org/10.1029/2005JD006318

Supporting Information for

Satellite-based assessment of methane emissions from the Darvaza gas crater

Adriana Valverde[1], Itziar Irakulis-Loitxate[2,1], Javier Gorroño[1], Zhipeng Pei[3], Javier Roger[1] and Luis Guanter[1,4]

[1] Research Institute of Water and Environmental Engineering (IIAMA), Universitat Politècnica de València, Spain

[2] International Methane Emission Observatory (IMEO), United Nations Environment Programme, Paris, France

[3] State Key Laboratory of Information Engineering in Surveying, Mapping and Remote Sensing, Wuhan University, Wuhan, China

[4] Environmental Defense Fund, Amsterdam, Netherlands

* Corresponding author's email: avaligl@doctor.upv.es

Contents of this file

Text S1 to S6

Figures S1 to S10

Tables S1 to S3

Introduction

This supplementary material provides additional information on analyzing methane emissions from the Darvaza crater.

Text S1. Topographic and geological contest of the Darvaza gas crater.

The topographic profile was generated using the SRTM 1 arc-second DEM from the USGS, with a spatial resolution of approximately 30 meters. This radar-derived dataset is well-suited for capturing elevation variations, such as the rim and internal depression of the Darvaza gas crater. Its consistent data quality enables a reliable representation of regional geomorphology despite the area's harsh surface conditions. The geological context shown in the plot (Figure S1) is based on the USGS geological map (Drummer, 1998), which complements the elevation data by delineating the surrounding sedimentary formations.

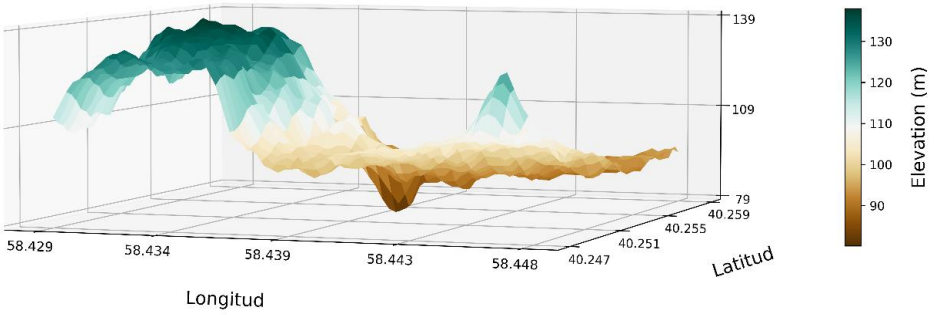

Figure S1. Elevation of the Darvaza gas crater area using the SRTM 1 arc.

Text S2. Thermal band selection for flaring detection.

In this study, we employed the thermal Band 7 (2.08–2.35 µm) and Band 6 (10.4–12.5 µm) of the Landsat 5 TM to detect and assess flaring activity within the crater (Figure S2). Band 7 was specifically utilized because its spectral range aligns with the peak thermal emission of typical gas flaring temperatures (~1500 K), as described by the Planck radiation law (Caseiro et al., 2018).

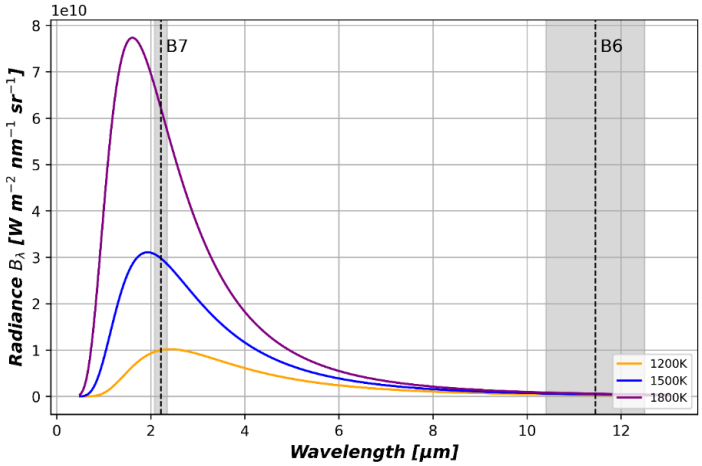

Figure S2. Plank curve for typical gas flaring temperatures and central wavelengths of Landsat 4-5 bands (B6, B7). The grey shaded areas indicate the full spectral bandwidth of each sensor band, while the vertical dashed lines represent their respective central wavelengths.

Text S3. Wind data sources.

ERA5-Land data were retrieved via Google Earth Engine (GEE) and are based on the climate reanalysis produced by the European Centre for Medium-Range Weather Forecasts (ECMWF) through the Copernicus Climate Change Service (C3S), providing high-resolution land surface variables from 1950 onwards (Figure S3; (Copernicus Climate Change Service, 2019)).

A comparative analysis was conducted between wind speed and wind direction data derived from the GEOS-FP and ERA5 datasets (Figure S4), given the critical role of atmospheric dynamics in accurately quantifying methane emissions. While some discrepancies were observed between the two sources, these differences did not influence the emission estimates significantly.

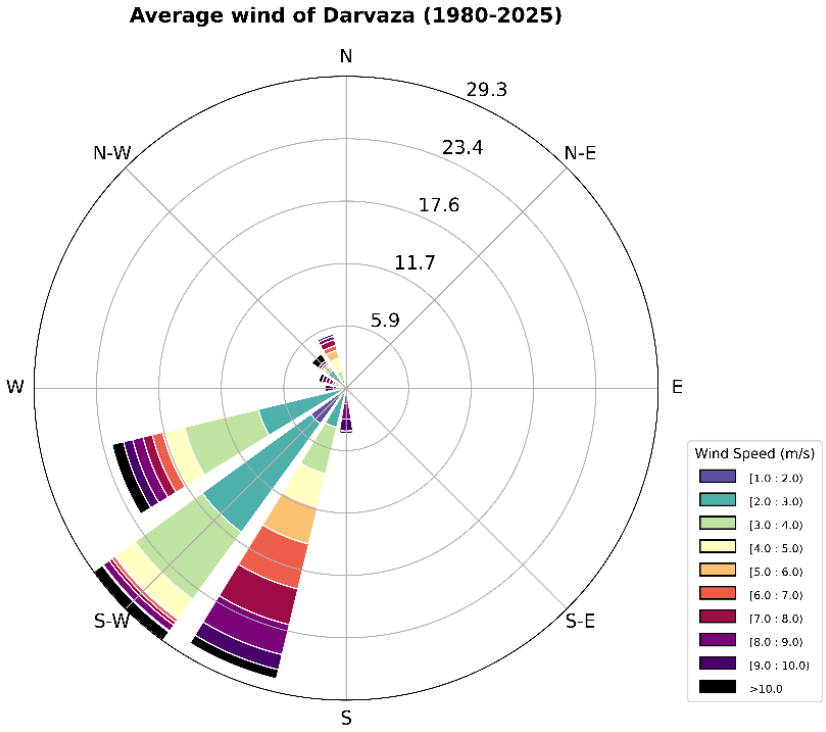

Figure S3. The average wind of the Darvaza gas crater area between 1950 and 2024 using the ERA-5 database. The numbers indicate the relative frequency of the direction of the wind.

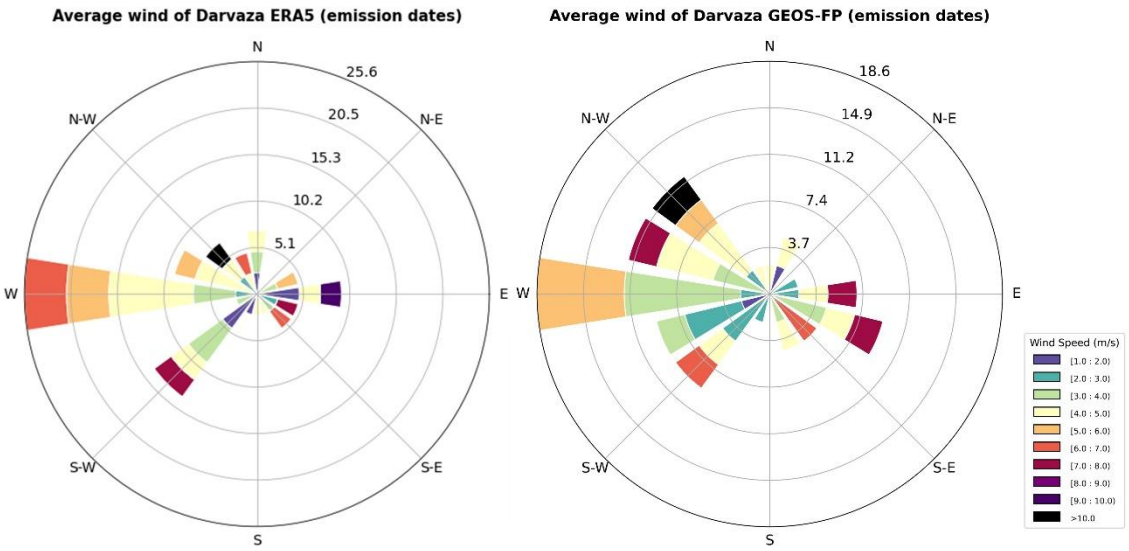

Figure S4. Comparison between wind speed and wind direction corresponding to the date of ERA-5 and GEOS-FP emissions. The numbers indicate the relative frequency of the direction of the wind.

Text S4. Hyperspectral acquisitions and methane plumes.

We have analyzed a dataset that includes 9 acquisitions from the ZY-1E hyperspectral mission, 2 from GF-5, 21 from PRISMA, 9 from EnMAP, and 20 from the EMIT instrument. Specifically, 44 images showed detectable methane emissions, 8 were partially or fully cloud-covered, 5 showed no detectable plumes, and 4 were out of the instrument's swath (Table S1). Acquisitions with methane plumes detected are listed in Table S2, while those without detected emissions are listed in Table S3. All these acquisitions have been visually analyzed, and the detected plume correlated with wind direction and speed. Additionally, throughout this research, acquisitions from the EnMAP and PRISMA satellites have been systematically requested, enabling the collection of multiple images captured on the same days by these two satellites and by EMIT (Figure S5). These multi-sensor observations enable cross-validation of methane emission estimates and demonstrate the consistency of detected plume structures across instruments.

Table S1. Summary of total hyperspectral satellite acquisitions over Darvaza.

SENSOR	Images	Emission	Cloudy	No plume	Out of swath
PRISMA	21	13	6	2	0
EnMAP	9	9	0	0	0
EMIT	20	14	2	0	4
ZY1-AHSI	9	6	0	3	0
GF5-AHSI	2	2	0	0	0
TOTAL	**61**	**44**	**8**	**5**	**4**

Table S2. Summary of the emissions rates from the high-resolution satellite observations. Q refers to the flux rates estimated for each plume in tonnes, and Q_err to the associated uncertainty in tonnes.

	DATE	SENSOR	Q (t/h)	Q_err (t/h)
1	2020-04-21	ZY1-AHSI	1.84	0.72
2	2021-10-09	PRISMA	0.91	0.40
3	2022-08-16	EMIT	1.06	0.50
4	2022-11-20	ZY1-AHSI	2.66	0.97
5	2023-03-29	EMIT	1.16	0.43
6	2023-04-18	EMIT	1.13	0.51
7	2023-06-13	EMIT	1.96	0.75
8	2023-06-13	ENMAP	1.36	0.53
9	2023-06-25	EMIT	1.31	0.48
10	2023-08-05	EMIT	2.23	1.03
11	2023-08-09	EMIT	1.81	0.73
12	2023-08-22	ZY1-AHSI	3.18	1.20
13	2023-08-25	EMIT	3.16	1.28
14	2023-10-16	ZY1	1.65	0.71
15	2024-02-01	EMIT	2.07	0.78
16	2024-03-26	EMIT	1.37	0.65
17	2024-03-29	ZY1-AHSI	1.16	0.50
18	2024-07-28	EMIT	0.63	0.23
19	2024-08-01	EMIT	1.12	0.44
20	2024-08-17	EMIT	0.94	0.40
21	2024-09-10	PRISMA	1.37	0.56
22	2024-09-14	ENMAP	1.75	0.68
23	2024-09-22	PRISMA	2.01	0.76
24	2024-09-22	ENMAP	1.42	0.53
25	2024-10-07	ENMAP	1.47	0.59
26	2024-10-15	ENMAP	1.22	0.42
27	2024-10-15	PRISMA	1.32	0.48
28	2024-11-02	PRISMA	0.81	0.32
29	2024-11-07	PRISMA	1.14	0.45
30	2024-11-07	ENMAP	1.26	0.49
31	2024-11-16	GF5-AHSI	2.51	1.02
32	2024-11-25	PRISMA	1.73	0.65
33	2024-12-06	PRISMA	1.14	0.40
34	2024-12-23	ENMAP	2.13	0.83
35	2025-01-10	PRISMA	1.54	0.49
36	2025-01-11	ZY1-AHSI	2.35	0.87
37	2025-01-28	PRISMA	2.31	0.92
38	2025-01-31	ENMAP	1.72	0.67
39	2025-02-14	PRISMA	0.91	0.27
40	2025-02-19	GF5-AHSI	0.82	0.22
41	2025-03-14	ENMAP	1.08	0.40
42	2025-03-15	PRISMA	1.59	0.65
43	2025-04-05	EMIT	1.14	0.49
44	2025-05-18	PRISMA	1.89	0.63

Table S3. Summary of the acquisitions with no-detected plumes from the high-resolution satellite observations and the corresponding wind speed from the GEOS-FP 1h reanalysis product.

	DATE	SATELLITE	WIND (m/s)
1	2020-08-18	PRISMA	1.57
2	2021-10-21	PRISMA	5.52
3	2023-12-23	ZY1-AHSI	4.91
4	2024-12-16	ZY1-AHSI	11.56
5	2024-12-29	ZY1-AHSI	4.88

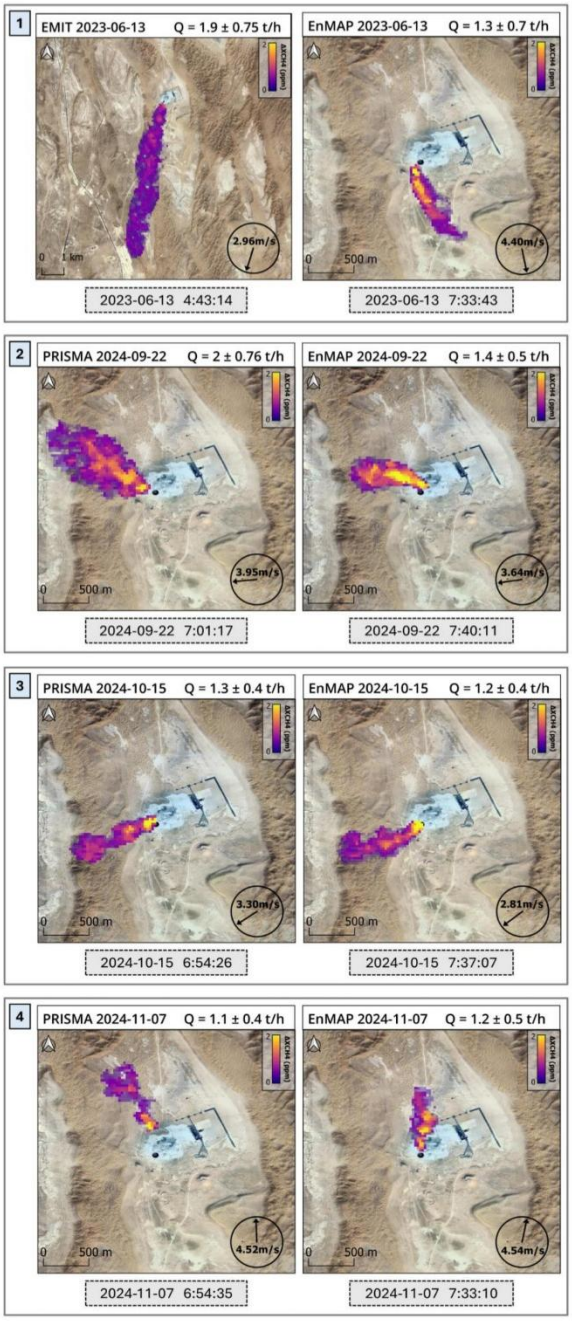

Figure S5. Comparison of methane plumes detected by EMIT, EnMAP, and PRISMA over Darvaza crater on four different dates. Each panel pair shows near-coincident acquisitions by EnMAP and either EMIT or PRISMA, illustrating spatial patterns of methane enhancements (ΔCH_4) and corresponding flux rates (Q, in t/h). Wind speed vectors used for flux quantification are indicated in the lower right of each panel. The timestamps at the bottom denote each image's acquisition time (UTC).

Text S5. Comparison of MODIS and VIIRS FRP data.

As shown in Figures S6 and S7, our time series analysis using MODIS Terra (2001–2019) and VIIRS (2012–2025) reveals that MODIS-derived FRP values are generally higher and exhibit greater temporal variability, whereas VIIRS data show lower, more stable values. These differences are primarily attributable to sensor-specific spatial and observational characteristics. MODIS, with its coarser 1-km resolution, integrates thermal signals over larger areas, often leading to overestimation of FRP in compact sources such as the Darvaza gas crater (~70 m in diameter). In

contrast, the 375-m resolution of VIIRS allows for more spatially refined detection of localized thermal anomalies, though it typically results in lower FRP values per pixel (Schroeder et al., 2014). Additionally, VIIRS exhibits greater sensitivity to low-intensity flares, with a minimum detectable FRP of ~0.4 MW, compared to ~2.5–17 MW for MODIS, depending on viewing geometry (Fu et al., 2020). Wooster et al. (2025) further emphasize that MODIS tends to overestimate FRP in small, hot sources due to broader pixel sampling and increased scene heterogeneity. These factors collectively explain the FRP differences observed between the two sensors at the exact location. The MODIS Terra record (Figure S6) shows remarkably stable FRP values with consistent seasonal peaks from 2001 through approximately 2019, with no discernible long-term decline. Both MODIS and VIIRS records exhibit clear seasonality, with higher FRP values during spring and summer and lower values in autumn and winter. This pattern is consistent across instruments and likely reflects seasonal variations in atmospheric transparency, viewing geometry, and surface thermal conditions rather than actual changes in gas flow or flaring activity. The decrease in MODIS Terra FRP after 2019 may be influenced by sensor degradation, known changes in the MODIS fire detection algorithm, and/or a real decline in flaring intensity, though VIIRS more clearly captures the latter. During the overlapping period (2012–2019), both datasets record consistent FRP levels, supporting the reliability of the observed flaring activity and confirming the absence of a significant declining trend before ~2018. The extended VIIRS record (Figure S7), which includes data from S-NPP (2012–2025), NOAA-20 (2018–2025), and NOAA-21 (2024–2025), reveals a gradual FRP decline beginning around 2018–2019, followed by an accelerated decrease after summer 2023, coinciding with reported mitigation efforts. Given these distinctions and the higher spatial resolution and sensitivity of VIIRS, we consider VIIRS data to be more reliable for flaring quantification.

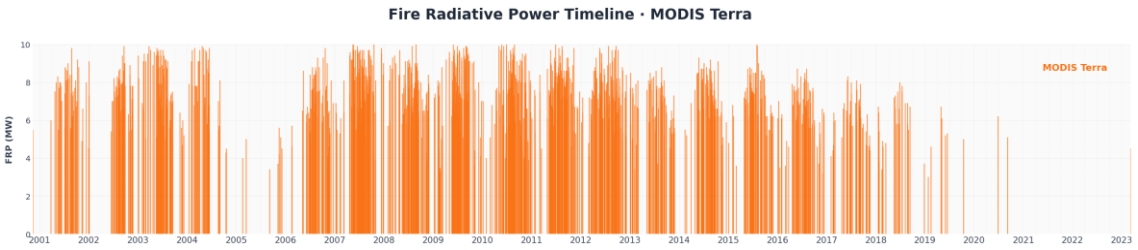

Figure S6. Flaring timeline using MODIS Terra from 2001 to 2020, showing Fire Radiative Power (FRP) values over nearly two decades of continuous monitoring.

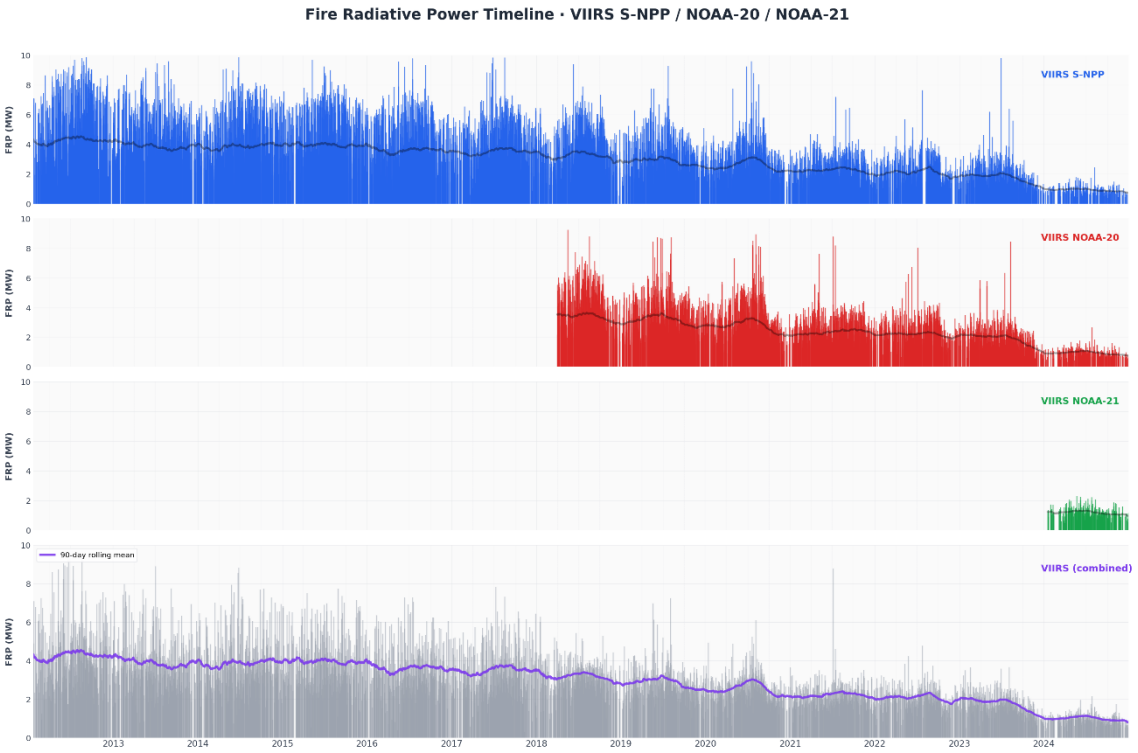

Figure S7. Flaring timeline using VIIRS from 2012 to 2025, including data from S-NPP, NOAA-20, and NOAA-21. The bottom panel shows the combined daily mean FRP across all three sensors with a 90-day rolling mean (purple line).

To assess the relationship between flaring intensity and methane emissions, we paired each satellite-derived methane flux measurement with the nearest daily mean VIIRS FRP value within a ±5-day window, yielding 32 coincident observations. A Spearman rank correlation test was performed, yielding $\rho = -0.003$ ($p = 0.989$), indicating no statistically significant relationship between FRP and methane emission rates (Figure S8). Methane plumes were detected during both high and low FRP periods, with comparable, though variable, emission rates in both cases. This result is consistent with the hypothesis that a significant fraction of methane reaches the atmosphere through diffuse subsurface venting pathways that bypass the active flame zone, decoupling methane emissions from flaring intensity.

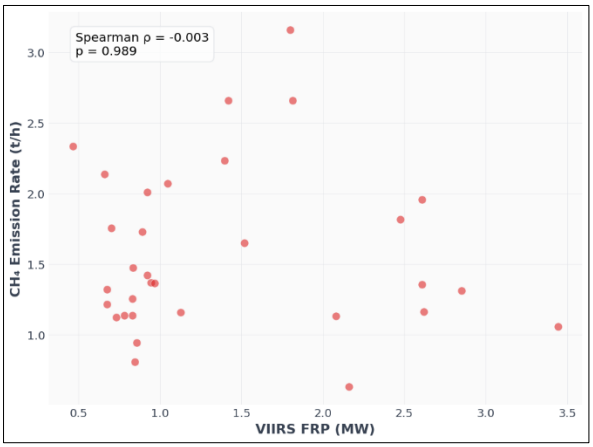

Figure S8. Scatter plot of VIIRS FRP versus methane emission rates for 32 coincident observations (±5-day matching window). Spearman $\rho = -0.003$, $p = 0.989$, indicating no statistically significant correlation.

Text S6. Total emission estimation.

In this study, we estimate that the total methane emissions from the Darvaza gas crater are 71 ± 21 kt CH_4 for the most recent period (2020–2025), based on plume detections derived from hyperspectral satellite observations. These estimates result from a second-order polynomial fit applied to 44 acquisition-derived flow rate measurements, with associated uncertainties represented by a 1σ confidence interval. The polynomial degree was selected using Leave-One-Out Cross-Validation (LOOCV), comparing degrees 1, 2, and 3. The resulting RMSE values were 0.584, 0.681, and 1.122 t/h, respectively (see Figure S9). Although degree 1 yields a marginally lower RMSE, the difference relative to degree 2 is small (0.097 t/h), and both models are statistically comparable in predictive performance. The degree 2 polynomial was selected because it better captures the expected non-linear temporal evolution of emissions from a depleting reservoir, where factors such as pressure decline, changes in subsurface venting pathways, and mitigation interventions may cause acceleration or deceleration over time. However, we acknowledge that the selection of fitting models introduces an additional source of error that is not explicitly accounted for.

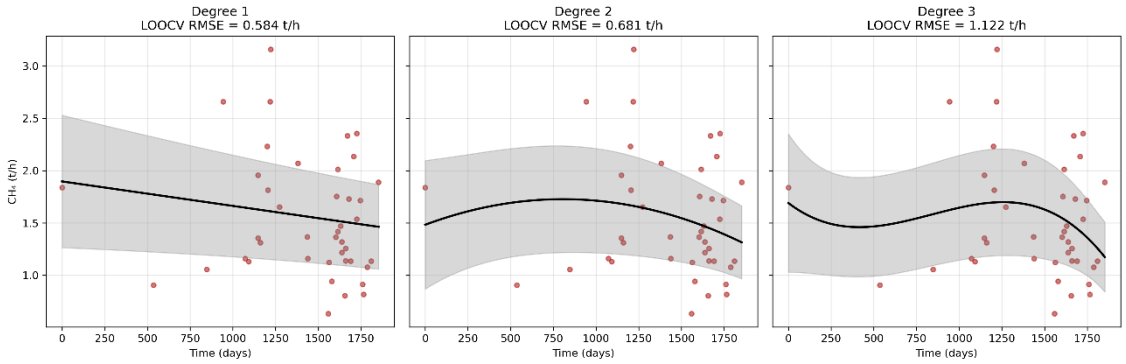

Figure S9. Comparison of polynomial fits (degrees 1, 2, and 3) applied to the full dataset (44 measurements, 2020–2025). Black lines represent the fitted trend, and grey shading indicates the ±1σ uncertainty band from the Monte Carlo analysis. LOOCV RMSE values are shown for each degree. Degree 2 was selected as the best compromise between physical plausibility and predictive performance.

To account for temporal variability and observational uncertainty, we employed a Monte Carlo approach that explicitly samples from each individual flow rate measurement within its respective noise level. For every acquisition, we defined the standard uncertainty as the product of the reported relative uncertainty and the flow rate. We then generated 10,000 realizations of a multivariate normal noise vector with zero mean and a covariance matrix constructed under the assumption of a constant inter-satellite error correlation of 0.5. Each noise realization was added to the original flow rates, and the same second-order polynomial fitting and integration procedure was applied to the perturbed data. The resulting probability distribution reflects both the trend in emissions and the propagated uncertainty over time (see Figure S10). To estimate cumulative emissions over the crater's full lifetime, we extrapolated the mean satellite-derived emission rate from 2020 to 2025 to the assumed formation date. The mean observed rate of approximately 1.5 t/h was applied as constant over the entire period, yielding cumulative estimates of approximately 800 ± 250 kt CH_4 for a 1971 formation date (54 years) and 900 ± 300 kt CH_4 for a 1963 formation date (62 years). The uncertainty was

propagated by scaling the relative uncertainty obtained from the Monte Carlo analysis. No distinction was made between the pre-flaring (1963/1971–1987) and flaring (1988–2019) periods, as no direct measurements are available for either interval. This approach is conservative, since during the pre-flaring phase, the absence of combustion would have led to the entire gas flux being vented directly into the atmosphere.

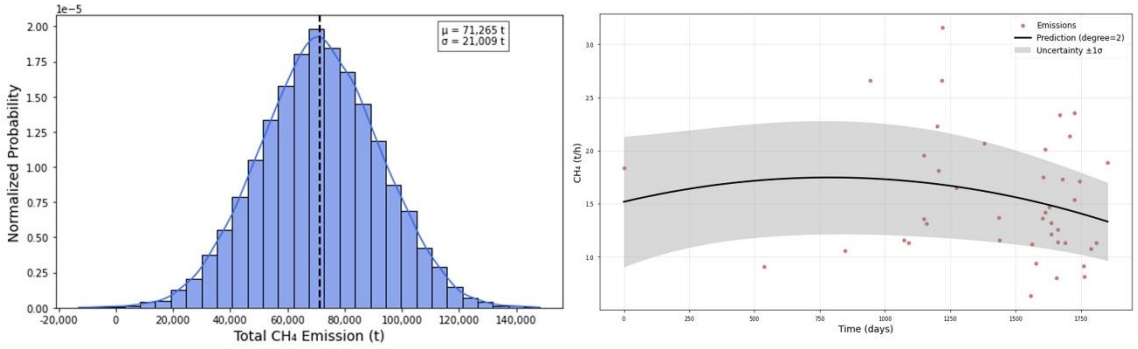

Figure S10. Total methane emissions. The upper graph presents a second-order polynomial fit to all satellites' 44 flow rate estimates. The grey-shaded region around the curve represents the uncertainty of the fit, corresponding to a coverage factor of k = 1. The lower graph displays the probability distribution function obtained by propagating both the temporal variation of the flow rate and its associated uncertainty through multivariate Monte Carlo simulations. In this process, an error correlation of 0.5 is assumed among the individual satellite observations.

Bibliography

Caseiro, A., Rücker, G., Tiemann, J., Leimbach, D., Lorenz, E., Frauenberger, O., & Kaiser, J. W. (2018, May 2). A Methodology for Gas Flaring Detection and Characterisation Using SLSTR. https://doi.org/10.20944/preprints201805.0020.v1

Copernicus Climate Change Service. (2019). ERA5-Land hourly data from 1950 to present [Data set]. Copernicus Climate Change Service (C3S) Climate Data Store (CDS). https://doi.org/10.24381/CDS.E2161BAC

Drummer, T. D. (1998). Generalized Geology of the Former Soviet Union (geo1ec) [Data set]. U.S. Geological Survey. https://doi.org/10.5066/P9GUL0PQ

Fu, Y., Li, R., Wang, X., Bergeron, Y., Valeria, O., Chavardès, R. D., et al. (2020). Fire Detection and Fire Radiative Power in Forests and Low-Biomass Lands in Northeast Asia: MODIS versus VIIRS Fire Products. *Remote Sensing*, *12*(18), 2870. https://doi.org/10.3390/rs12182870

Schroeder, W., Oliva, P., Giglio, L., & Csiszar, I. A. (2014). The New VIIRS 375 m active fire detection data product: Algorithm description and initial assessment. *Remote Sensing of Environment*, *143*, 85–96. https://doi.org/10.1016/j.rse.2013.12.008

Wooster, M. J., Roberts, G., Perry, G. L. W., & Kaufman, Y. J. (2005). Retrieval of biomass combustion rates and totals from fire radiative power observations: FRP derivation and calibration relationships between biomass consumption and fire radiative energy release. *Journal of Geophysical Research: Atmospheres*, *110*(D24), 2005JD006318. https://doi.org/10.1029/2005JD006318